https://doi.org/10.1016/j.nanoen.2020.105606

Atomically Targeting NiFe LDH to Create Multivacancies for OER Catalysis with a Small Organic Anchor

Yaqiong Wang[1], Shi Tao[3], He Lin[2], Gaopeng Wang[1], Kangning Zhao[4], Rongmin Cai[1], Kewen Tao[1], Chengxu Zhang[5], Mingzi Sun[6], Jue Hu[5*], Bolong Huang[6*] and Shihe Yang[1,2*]

[1]*Guangdong Key Lab of Nano-Micro Materials Research, School of Chemical Biology and Biotechnology Shenzhen Graduate School, Peking University, 518055 Shenzhen, China.*

[2]*Department of Chemistry, The Hong Kong University of Science and Technology, Clear Water Bay, Kowloon, Hong Kong, China.*

[3]*School of Electronic and Engineering, Jiangsu Laboratory of Advanced Functional Materials, Changshu Institute of Technology, Changshu 215500, China.*

[4]*College of Sciences and Institute for Sustainable Energy, Shanghai University, Shanghai, 200444, China.*

[5]*Faculty of Science, Kunming University of Science and Technology, Kunming, 650093, China.*

[6]*Department of Applied Biology and Chemical Technology, the Hong Kong Polytechnic University, Hung Hom, Kowloon, Hong Kong SAR, China.*

Correspondence Email: hujue@kust.edu.cn (J. Hu); bhuang@polyu.edu.hk (B. Huang); chsyang@pku.edu.cn (S. Yang)

Keywords : layered double hydroxide, methyl-isorhodanate, targeted atoms, multivacancies, oxygen evolution reaction

Abstract

The fabrication of porous structure in the ultrathin materials still faces high difficulties. In particular, the precise modulations in the porosity and size are highly challenging. In this work, we have introduced the small molecules to overcome such a challenge. And this substantially contributes to the energy related applications, especially to the water-energy (WE) treatment. Electrocatalytic water-splitting is hindered by the sluggish kinetics of water oxidation, requiring efficient earth-abundant electrocatalysts for the oxygen evolution reaction (OER). Herein we demonstrate the robust OER activity by introducing metal and oxygen multivacancies in noble-metal-free layered double hydroxides (LDHs) through the specific electron-withdrawing organic molecule methyl-isorhodanate (CH_3NCS). Our work reveals that the metal and oxygen vacancies endow NiFe LDH with enhanced electron transfer and modulate the H_2O adsorption, thereby boosting the OER electrocatalytic properties. Remarkably, the best-performing laminar NiFe LDH nanosheets with metal and oxygen multivacancies (*v*-L-LDHs) shows an ultra-low overpotential of 230 mV at 100 mA cm^{-2} and Tafel slope of 37.1 mV dec^{-1}. Density functional theory (DFT) has revealed the improved OER performance is realized by the co-existence of metal and O vacancies in NiFe LDH, where the defective region activates the electroactivity of Ni sites and O sites to promote the electron transfer and intermediate transformation. The Fe sites play a key role to preserve the high electroactivity of the Ni sites in long-term applications. The superior OER performance underpins the high potential of the reported facile organic anchor strategy for designing and synthesizing advanced electrocatalysts in both LDH and other potential 2D layered materials.

Introduction

Hydrogen production by water splitting is one of the most promising ways to tackle the approaching energy crisis and environmental problems.[1] In this process, the oxygen evolution reaction (OER) is the rate-determining half-reaction.[2-3] Therefore, efficient and low-cost oxygen evolution catalysts that could greatly accelerate the intrinsically sluggish kinetics and lower the unacceptable overpotential of OER are of key importance.[4-5] Owing to relatively low cost, earth-abundant, and high catalytic activity,[6-9] layered double hydroxides (LDHs), formulated as $[M^{2+}_{1-x}M^{3+}_{x}(OH)_2]^{x+}(A^{n-})_{x/n}\cdot mH_2O$, is a promising alternative to RuO_2 and IrO_2 for catalyzing electrochemical oxygen (O_2) production from water.

LDHs are two-dimensional lamellar ionic crystals consisting of positively charged brucite-like host layers and exchangeable charge-balancing interlayer anions.[8, 10] The host layer was composed of edge-sharing octahedral MO_6 units, which have been known as active sites.[11-13] To enhance the OER catalytic activities of LDHs, one strategy is focused on exposing edge sites maximally employing ultrafine LDHs[14] and vertical nanoflakes[15]. Another strategy strives to improve the intrinsic active sites by atomic-scale modification of catalytic sites with lower coordination numbers and more dangling bonds.[16-17] Presence of vacancies in catalysts can impressively modulate the local atomic structure, which tunes the electronic configuration on the surface and creates an unsaturated coordinative geometry.[18-22] Compared to anion or cation vacancy alone, a combination of the anion and cation multivacancies often produces synergy for the enhanced electrochemical activity.[18, 20, 23-24] For example, Wang and co-workers firstly engineered the CoFe bulk LDH to be dry-exfoliated by Ar-plasma and then produced multiple vacancies (including O, Co, and Fe vacancies) in the ultrathin 2D nanosheets.[25] Recently, novel technologies, such as laser and flame,[26-27] have shown their potential for generating vacancies in applications. However, the basic principles of generating vacancies were still unknown and could not be controlled quantitatively. Zhang and co-workers generated monolayer NiFe LDH with multiple kinds of vacancies of Ni, Fe, and O via high concentration salts at pH = 10 achieving an improved electrical conductivity, larger electrochemical surface area (ECSA), and faster charge transfer compared to bare LDH.[28] However, the methods of creating multivacancies are still random and limited to monolayer LDHs. Besides, few approaches have sought to consider the multilayered materials and make vacancies on the basal plane that constitutes the majority of the layered materials. To fully utilize common LDH materials, specific methods for activating the basal plane of layered materials are still needed.

Herein, we report a facile way to successfully optimize the edge and basal plane of LDHs by creating metal and oxygen multivacancies based on a small organic molecule methyl-isorhodanate (CH_3NCS) elaborately. In the octahedral MO_6 layer structure of LDH, the nucleophilic group -OH is expected to interact with organic receptors. According to the common interlayer spacing of LDH (≈ 0.7 nm), a size-matched electron-withdrawing organic molecule CH_3-N=C=S (a ≈ 0.278 nm, b ≈ 0.254 nm, c ≈ 0.557 nm from theoretical calculation, see Fig. S1) was selected as the anchoring agent. The CH_3NCS molecules were able to break into the interlayers of LDH and anchored onto specific atoms (oxygen and metal atoms) of the

MO_6 units in the LDH matrix. This led to exfoliation of the LDH nanosheets, and subsequent withdrawal of the CH_3NCS together with the hooked atoms, which resulted in the successful formation of oxygen and metal multivacancies. The optimized laminar NiFe LDH catalyst with multivacancies yields high OER activity with an overpotential as low as 150 mV at 10 mA cm^{-2}, which is superior to most previously reported earth-abundant OER catalysts. DFT calculations confirm that the synergic effect between the metal vacancies and the O vacancies in the NiFe LDH for promoting the electron transfer with the alleviated barrier of electron transfer. Such a combined defective region not only facilitates the electroactivity but also the stabilization of intermediates. The modulated electronic environment determines superior OER performance.

Results and Discussion

Design of the NiFe LDH with Metal and OH Multivacancies

We have applied the DFT calculations to unravel the vacancy induced modulation of the OER performance in NiFe LDH. For the formation of vacancies, we have considered several possible situations to compare their electronic structures modulated by different vacancies (**Fig. 1A-D**). For the NiFe LDH with only the surface oxygen vacancy, the bonding and anti-bonding near the Fermi level (E_F) demonstrate the electroactive region near the oxygen vacancies. For the metal vacancies, the even stronger perturbation to the electronic distribution of lattice is observed, which modulates the surface of NiFe LDH to be more electron-rich. The metal sites near the vacancy dominate the main electronic contribution near the EF. Meanwhile, the metal vacancies induce more evident lattice distortions to the nearby lattice, where the directions of neighboring *OH groups become deviated. For the coexistence of both metal vacancies and oxygen vacancies, the electroactive region has been further localized near the defective region, which supplies the active region for the OER process. Then, we further investigate the partial density of states (PDOSs) of the NiFe LDH with the co-existence of metal and oxygen vacancies (*v*-NiFe LDH) (**Fig. 1E**). The dominant peak of Ni-3d orbitals locate at E_V-1.70 eV and the peak positions of the t_{2g} and e_g components in Fe-3d orbitals occupy E_V-3.30 eV and E_V+0.40 eV, respectively (E_V = 0 for EF). The O-2p orbitals indicate an electron-rich feature in a deeper position. Moreover, Ni-3d and Fe-3d orbitals show the well overlap with O-2p orbitals to support the sufficient site-to-site electron transfer and stable bonding. The site-to-site PDOSs of each element is also demonstrated to compare the vacancy induced difference in electronic structures (**Fig. 1F**). For Ni-3d orbitals, the gradual upshifting trend of 0.44 eV for the Ni sites from the bulk to the Ni sites near the vacancies, indicating an improved electron transfer capability and higher bonding trend with the adsorbates. For the Fe-3d orbitals, we noticed the pinned positions of t_{2g} and e_g components in the lattice, which demonstrates a crucial role to preserve the Ni oxidation states and the electron-transfer activities (**Fig. 1G**). The O-sites also demonstrates a more evident upshifting trend from EV-5.50 eV and EV-4.10 eV, supporting the alleviated electron transfer barrier from O sites to the neighboring metal sites, indicating a high electroactivity. The potential activation and exchange of *OH in *v*-NiFe LDH are also possible (**Fig. 1H**). In addition, the intermediates of OER is investigated. From the initial reactants *OH towards the final product O_2, a linear correlation is explicitly displayed, which guarantees the efficient electron transfer and intermediate transformation during the OER (**Fig. 1I**).

NiFe LDH is one of the most promising electrocatalysts for OER, and composed of cationic metal atom inner layers sandwiched between the two intercalated anionic layers. The cationic layer in the LDH matrix consists of octahedral structural unit (MO_6) with four −OH owning lone pair and one transition metal in a plane, and another two −OH at the vertices.[29] In view of the electrophile properties of methyl isothiocyanate ($CH_3N=C=S$) as electron acceptor, the lone pair in −OH group of LDH would primarily attack the electrophile center-Carbon (4+) of −N=C=S, as schematically illustrated in **Fig. 2A**. At the same time, the terminal sulfur of −N=C=S would target to the metal atom in MO_6, forming the possible structure II (**Fig. 2A**). The unstable structure II was isomerized to corresponding methyl carbamothioic acid S-metal complex (Structure III). Afterwards, the metal-organic complex (structure III) were wiped off due to its moderate solubility in organic reagent such as ethanol,[30] and as a result, the metal and oxygen multivacancies were created in the LDH matrix (denoted as *v*-NiFe LDH), and led to exfoliation of the LDH nanosheets. The charge was possibly balanced by the reduced intercalated anion derived from the decreased thickness. In order to determine the structure of the metal-organic complex (structure III), the ethanol scrubbing solution (Fig. S2) was carefully characterized by inductive coupled plasma emission spectrometer (ICP), X-ray photoelectron spectroscopy (XPS), nuclear magnetic resonance (^{1}H-NMR), ^{13}C-NMR, and mass spectra (MS). From the ICP results of ethanol scrubbing solution (Table S1), accordantly, the concentration of Fe element was detected to 4.96 mg/L, and that of Ni was 47.86 mg/L, confirming the transition metal ions were wiped off by ethanol in a convenient way. The guiding agent CH_3NCS was effective to create metal vacancies, thus the material LDH targeted by CH_3NCS was denoted as *v*-NiFe LDH.

X-ray photoelectron spectroscopy (XPS) were applied to further examine elaborately the species of metal ions and sulfur in scrubbing solution. The high resolution XPS Ni 2p spectra could be fitted with two distinct doublets ($2p_{3/2}$ and $2p_{1/2}$): one doublet at about 856.1 eV and 874.2 eV, which reflected the Ni-O,[31] and the other doublet at about 853.4 eV and 871.7 eV, which ascribed to the Ni-S (**Fig. 2C**).[32] The high resolution XPS Fe 2p spectra could also be fitted with two distinct doublets ($2p_{3/2}$ and $2p_{1/2}$): one doublet at about 711.3 eV and 724.7 eV, which reflected the Fe-O,[33] and the other doublet at about 713.8 eV and 721.8 eV, which ascribed to the Fe-S (Fig. S3).[34] The formation of Ni-S and Fe-S demonstrated that the sulfur in CH_3NCS was successfully coordinated with the Ni and Fe metal atoms in NiFe LDH, which in corroboration with the proposed mechanism (**Fig. 2A**). Meanwhile, from the high resolution XPS S 2p spectrum in Fig. 2B, three types of S were conducted and each type with two peaks attributed to S $2p_{3/2}$ and S $2p_{1/2}$ respectively. The peaks at 168.1eV and 169.2eV corresponded to isothiocyanate, of which S 2p of solid CH_3NCS was shown in Fig. S4 as reference. The appearance of Ni-S at 162.2 eV[35] and 163.4 eV and the formation of NHOC-S at 164.8 eV[36] and 166 eV for S $2p_{3/2}$ and S $2p_{1/2}$, respectively well proved the above-proposed structure III.

In order to get more detailed information about the structure of the wiped off complex, NMR was carried out. From the ^{1}H-NMR (**Fig. 2E**), the obvious peak at around 3.4 ppm was according to the solvent MeOD.[37] The peak located at around δ 2.9 ppm and 4.5 ppm were ascribed to the H of $–CH_3$[38] and the H of $–NHCH_3$[39], respectively. The integral data of

these two peaks were 3 and 1, respectively, which was in agreement with the structure Ⅲ. The ^{13}C-NMR (**Fig. 2F**) result is in well consistent with that of ^{1}H-NMR, which exhibited the peaks at δ 29 ppm and 209 ppm were evidently attributed to $-CH_3$[40] and −NHCO[41], respectively, confirming structure III was wiped off from the LDH matrix.

Furthermore, mass spectrometry (MS) was used to finally check the structure Ⅲ and the results are shown in **Fig. 2D**. Theoretically, the accurate molar masses of structure Ⅲ coordinated with Ni^{2+} and Fe^{3+} were 164.9394 and 162.9766 respectively. Two major peaks found in the MS in **Fig. 2D** were at *m/z* values of 165.9079 and 163.9129 assigned to the proton combined structure III coordinated with Ni^{2+} and Fe^{3+}, respectively. The full spectrum spanning *m/z* values of 100 and 1000 is shown in Fig. S5, most of the peaks were assigned to structure III with Ni^{2+} and Fe^{3+} in different types, and two minor impurity peaks located at *m/z* values of 139.0629 and 302.8701. The MS results were in good agreement with the analyses of ICP, XPS and NMR, further confirming the methyl carbamothioic acid S-metal complex (structure III) generated and wiped off from the LDH matrix shown in **Fig. 2A**.

For comparison, under the same condition without the organic molecular anchor, the experiment was conducted, and the scrubbing solution was analyzed by XPS, ICP, NMR, and MS. The results of Fe 2p XPS (Fig. S6A) exhibited one doublet at about 711.1 eV and 724.7 eV, which reflected the Fe-O,[33] and the Ni 2p XPS (Fig. S6B) also exhibited one doublet at about 856.1 eV and 874.2 eV, which reflected the Ni-O. The peaks rooted in the slight solubility of NiFe LDH in solvent and there were no metal-S peaks, which confirmed the emerging metal-S peaks in the scrubbing solution of NiFe LDH treated by CH_3NCS (vide supra) derived from the role of CH_3NCS. And a very low quantity of Fe (0.083 mg/L) and Ni (0.488 mg/L) detected in the scrubbing solution using ICPs shown in Table S2 further demonstrated only slight dissolution of NiFe LDH. In Fig. S7, from the ^{1}H and ^{13}C NMR spectrum, exhibited the peaks at around δ 3.3 ppm and 49 ppm respectively, were evidently attributed to pure solvent MeOD[37] indicating no metal-complex was formed. The MS result (Fig. S8) showed that the major peaks at m/z values at 139.0729 and 301.1408 were assigned to the impurity peaks which also existed in the slurry of LDH targeted by CH_3NCS (Fig. S5). These results all confirmed the multivancies in *v*-NiFe LDH rooted in the eliminated anchored atoms targeted by organic molecular CH_3NCS.

Morphology and Structure of NiFe LDH with Metal and Oxygen Multivacancies

Even that, judging from the scanning electronic microscopy (SEM, Fig. S9A&B), the nanosheet structures were kept well and have no obvious distinction before and after CH_3NCS targeted. From X-ray diffraction (XRD) pattern in Fig. S10, all the peaks of NiFe LDH were well indexed to LDH (JCPDF no. 38-0715) and the peaks of *v*-NiFe LDH almost had no change, demonstrating that the crystal structure basically remained unchanged. Conceivably and precisely, from transmission electron microscopy (TEM) images shown in **Fig. 3C&D** and Fig. S11, indeed the nanosheet morphology was kept well, merely the thickness of the

nanosheets decreased from around 8 nm to 2.5 nm. Atomic force microscopy (AFM) was also carried out to determine the specific thickness of the *v*-NiFe LDH nanosheets (**Fig. 3E&F**), which were even more dispersed and found to have a uniform thickness of ≈ 4 nm. This thickness was much smaller than that of NiFe LDH (≈ 10 nm), in agreement with TEM analysis. The size of *v*-NiFe LDH nanosheet was smaller than NiFe LDH, specifically facilitating in exposing more electrocatalytic active sites with numerous coordinated unsaturated sites.[42] It was possible that the molecular CH_3NCS inserted into the interlayer and targetedly etched the specific atoms, due to the perfectly matched size of CH_3NCS with cell parameter c ≈ 5.58 Å (Fig. S1), lower than the interlayer spacing 7.8 Å calculated by XRD and the flexible structure of the layer material.

More noteworthy, on account of wiped off metal complex, the vacancies were created as expected, accompanied by lattice distortion to accommodate the change in the electronic environment. This was borne out directly from high resolution transmission electronic microscopy (HRTEM) images (**Fig. 3A&B**), wherein distortions could be found in *v*-NiFe LDH (**Fig. 3B**, red circles), instead of the continuous lattice fringes for NiFe LDH (Fig. 3A), suggesting the atomic structure modulation effect of the successful CH_3NCS targeting and etching. The XPS S 2p spectra of the NiFe LDH and *v*-NiFe LDH were conducted and shown in Fig. S12. No peaks were exhibited for both the NiFe LDH and *v*-NiFe LDH samples, confirming that the metal-organic complex (structure III) containing sulfur were washed thoroughly

In order to check the existence of the O vacancies, the O1s XPS data were conducted and likewise indicated the formation of O vacancy arising from the ligand change from hydroxide to sulfur complex in NiFe LDH and then wiped off by ethanol (**Fig. 4A&B**). The high-resolution O 1s spectra of NiFe LDH (**Fig. 4A**) revealed four distinct peaks attributed to the surface hydroxyl groups attached to metal-oxygen (531.5 eV), lattice oxygen (530.5 eV), under coordinated lattice oxygen related to oxygen vacancies (531.6 eV), and adsorbed water (532.8 eV).[43] In **Fig. 4B**, the intensities of oxygen vacancies and adsorbed water of *v*-NiFe LDH enhanced compared to those of NiFe LDH, indicating the formation of O vacancies. From the total content analysis from XPS shown in Table S3, the oxygen decreased from 57.93 % to 54.46 %, an indication of the loss of oxygen atoms in the *v*-NiFe LDH sample, suggesting the generation of oxygen vacancies.

As for the metal vacancies, XAS analysis was employed to reveal the local chemical and electronic environment of the *v*-NiFe LDH material. The K-edge k^3x oscillation curve of Ni-K edge (**Fig. 4E**) and Fe-K edge (**Fig. 4F**) in *v*-NiFe LDH were both demonstrated subtle reductions in the oscillation amplitudes, suggesting a coordination environment change for the Ni and Fe atoms compared to the NiFe LDH. Furthermore, the fourier-transformed k^3x functions, shown as the Ni-R space curve (**Fig. 4G&I**, Table S4), gave the detailed information about Ni coordination, such as the average distance (*R*), and the calculated coordination number (*N*) of the first Ni-O shell and the second Ni-Ni/Ni-Fe shell. The coordination number (*N*) of Ni-Ni/Ni-Fe decreased from 7.6/1.5 for NiFe LDH to 6.8/1.4 for *v*-NiFe LDH, indicating

that *v*-NiFe LDH was rich in Ni and Fe vacancies. Similarly, in **Fig. 4H&J**, Table S5, the *N* of Fe-Fe/Fe-Ni shell reduced from 6.9/1.4 to 6.5/1.3, also resulting from severe metal vacancies in *v*-NiFe LDH. Despite the metal vacancies, the oxygen vacancies were further confirmed. Compared with the *N* (6.0) of Ni-O shell in NiFe LDH, the Ni-O shell for *v*-NiFe LDH had a lower amplitude and *N* (5.3), indicating severe structural distortion derived from abundant of oxygen vacancies (V_O) in *v*-NiFe LDH (Table S4). Similarly, in **Fig. 4H&J**, Table S5, the N of Fe-O shell was reduced from 5.9 for NiFe LDH to 5.6 for *v*-NiFe LDH, confirming the oxygen vacancies exited in *v*-NiFe LDH. The K-edge X-ray absorption near-edge structure (XANES) spectra of Ni (**Fig. 4C**) and Fe (**Fig. 4D**) in *v*-NiFe LDH suggested a reduced valence state of the Ni and Fe components, which was attributed to the presence of oxygen vacancies. **Fig. 4K** showed the schematic process changing from thick NiFe LDH to thin *v*-NiFe LDH with oxygen and metal multivacancies, both of which could be expected extraordinarily to alter the typical LDH electronic structural and enhance the electrocatalytic performance for water splitting.

Electrocatalytic OER Activity

According to the linear sweep voltammetry (LSV) data (**Fig. 5A**), the original NiFe LDH exhibited a low overpotential of 350 mV at a current density of 50 mA cm^{-2}, which was consistent with the general reported performance.[44] In order to exclude the contribution of the Ni form to the OER performance, the LSV of Ni form was also conducted and shown in Fig. S13, exhibiting the overpotential at 10 mA cm^{-2} was 410 mV. The *v*-NiFe LDH showcased excellent OER activity as evidenced by an overpotential (η) of only 260 mV at a current density of 50 mA cm^{-2} and knockdown Tafel slope of 34.8 mV dec^{-1} (**Fig. 5B**), which were much lower than the values of the original NiFe LDH (350 mV of potential and 63.8 mV dec^{-1} of Tafel slope). In order to get known to the origin of the outstanding OER activity of *v*-NiFe LDH, electrochemical impedance spectroscopy (EIS) was conducted to study the electron transfer resistance for *v*-NiFe LDH during electrochemical reaction. As shown in Fig. 5C, *v*-NiFe LDH had a remarkably smaller charge transfer resistance compared with NiFe LDH, the increased disorder and homogeneity of *v*-NiFe LDH are possible reasons for its larger charge transfer resistance. The electrochemical active surface area (ECSA) of LDH and *v*-NiFe LDH was also measured (Fig. S14). The ECSA of *v*-NiFe LDH was determined to be 5.47 mF cm^{-2}, larger than that of NiFe LDH (4.36 mF cm^{-2}), clearly, the NiFe LDHs etched by CH_3NCS offered a larger electroactive surface for OER, thereby making an important contribution to its outstanding OER activity.

The content of multivacancies of LDHs could be gradually changed and varied by different concentrations of guiding agent CH_3NCS and have effect on the OER performance. The ICP measurements were conducted semi-quantitatively (Table S6) related to multivacancies. When the concentration of CH_3NCS was up to 0.5M, the OER reached to the highest current density(Fig. S15). What's more, the similar structure CH_3-S-C≡N nevertheless with no terminal sulfur and CH_3−C≡N with no double bonds were also applied as guiding agent to etch

LDHs, respectively. The scrubbing solvents were both transparent which were very district from the phenomenon $CH_3N=C=S$ targeted. Thus, the terminal sulfur and the special double bonds of the −N=C=S had significant effect on anchoring elaborately on the specific atoms and etching. In additional, the LSVs were conducted by LDHs treated by $CH_3-S-C\equiv N$ and $CH_3-C\equiv N$ (Fig. S16). The OER activities were even worse with the Tafel slope of 69.1 and 71.9 mV dec^{-1}, respectively compared with NiFe LDH with Tafel slope of 65.5 mV dec^{-1}, confirming that the vacancies were not be created, further suggesting that the structure of $CH_3-N=C=S$ has a crucial role on the elaborated targeting and etching LDHs to create multivacancies.

The *v*-NiFe LDH also exhibited a good durability for OER. As shown in Fig. 5D, over the duration more than 30 hours, the anodic potential required to maintain an anodic current density of 50 mA cm^{-2} for *v*-NiFe LDH catalyst exhibited just 5.7 % lost. The benign durability was further proved by the comparison of OER performance before and after 2000 cycles. The OER performance was almost the same (inset of Fig. 5D). Moreover, both the micro-morphology (Fig. S17) and atomic structure (Fig. S19, Fig. S20) of *v*-NiFe LDH after the stability tests were kept well. Furthermore, Both the Ni^{3+} and Ni^{2+} could be deconvoluted from the high resolution XPS spectra in the Ni region for both *v*-NiFe LDH before (Fig. S20A) and after CP testing (Fig. S20B), the ratio of Ni^{3+}/Ni^{2+} has no change, exhibiting the long-term stability of *v*-NiFe LDH for OER catalysis. Meanwhile, the faradaic efficiency (FE) of the OER on *v*-NiFe LDH was tested to be ≈ 97.1 % (**Fig. 5E**), suggesting the high efficiency of energy conversion capability of *v*-NiFe LDH

In order to directly understand the effect of multivacancies of LDHs on the OER performance, decreasing the thickness of LDH was expected to eliminate the disturbance of interlayer spacing or interlayer anion as much as possible. Herein, the lamina LDH with few layers was further synthesized and denoted as L-LDH.[45] Atomic force microscopy (AFM) was carried out to determine the thickness of the L-LDH nanosheets (**Fig. 6A**, Fig. S21A). The nanosheets were found to have a uniform thickness of ≈3 nm (**Fig. 6C**, Fig. S21D). According to the same method above-mentioned, L-LDH was targeted by CH_3NCS, the *v*-L-LDH was obtained and detected by AFM (**Fig. 6B**, Fig. S21B&C). The very uniform nanosheets were found to have a thickness of just ≈ 1.0 nm (**Fig. 6D**, Fig. S21E&F), further confirming CH_3NCS inserted into L-LDH as above-proposed mechanism. Notably, *v*-L-LDH showed an extraordinary low overpotential of 150 mV at the current density of 10 mA cm^{-2} and exhibited a very low Tafel slope of 37.1 mV dec^{-1}, superior to previous works shown in Table S7. Furthermore, the stability of *v*-L-LDH was also conducted by chronopotentiometry at 20 mA cm^{-2} (**Fig. 6H**). Over the duration more than 60 hours, the anodic potential was kept well, meanwhile, the OER performance was substantially unchanged. Furthermore, after elevating the current density to 50 mA cm^{-2} conducted by CP testing, the potential was also kept well which was shown in Fig. S22. And both the Ni^{3+} and Ni^{2+} could be deconvoluted from the high resolution XPS spectra in Ni region for both *v*-L-LDH before (Fig. S23A) and after testing (Fig. S23B), the ratio of Ni^{3+}/Ni^{2+} also has no change, exhibiting a striking durability.

To access the generality of the role of CH_3NCS on TM LDHs, NiCo and CoFe LDHs were also treated with CH_3NCS by the same procedure. The scrubbing solutions were conducted by XPS and MS, meanwhile the electrocatalytic performances of the materials were also carried out.

Both the Ni-O and Ni-S could be deconvoluted from the high resolution XPS spectrum in the Ni region for NiCo LDH (Fig. S24A). Meanwhile, the high resolution XPS Co 2p spectrum (Fig. S24B) could also be fitted with three distinct doublets ($2p_{3/2}$ and $2p_{1/2}$): one doublet at about 782.5 eV and 798.3 eV, which reflected Co^{2+},[46] and one doublet at about 780.9 eV and 796.8 eV,[46] which ascribed to Co^{3+}, and the other doublet at about 779.5 eV and 795.1 eV, which corresponded to Co-S.[47] The formation of Ni-S and Co-S demonstrated that the sulfur in CH_3NCS could be successfully coordinated with the Ni and Co atoms in NiCo LDH, which in corroboration with the proposed mechanism (**Fig. 2A**). Two major peaks found in the MS spectrum in Fig. S25A were at *m/z* values of 165.9088 and 167.0004 assigned to the proton combined structure III coordinated with Ni^{2+} and Co^{3+}, respectively. The electrocatalytic performance of NiCo LDH reacted by CH_3NCS denoted as *v*-NiCo LDH were conducted by LSV (Fig. S26). The *v*-NiCo LDH showed a slight lower overpotential of 370 mV at the current density of 10 mA cm^{-2} compared with NiCo LDH of 390 mV and exhibited a slight lower Tafel slope of 60.8 mV dec^{-1}, superior to NiCo LDH (62.8 mV dec^{-1}).

As for the scrubbing solution of CoFe LDH after treated by CH_3NCS, the high resolution XPS Co 2p spectrum (Fig. S27A) could also be fitted with three distinct doublets ($2p_{3/2}$ and $2p_{1/2}$) corresponding to Co^{3+}, Co^{2+}, and Co-S, respectively, which was similar to the Co 2p XPS spectrum of NiCo LDH. And the high resolution XPS Fe 2p spectrum could also be fitted with two distinct doublets ($2p_{3/2}$ and $2p_{1/2}$): one doublet at about 711.1 eV and 724.7 eV, which reflected the Fe-O,[33] and the other doublet at about 713.8 eV and 721.8 eV, which ascribed to the Fe-S (Fig. S27B).[34] The theoretical accurate molar masses of structure Ⅲ coordinated with Co^{2+} and Fe^{3+} were 165.9373 and 162.939. Two major peaks found in the MS spectra in Fig. S28A were at *m/z* values of 167.0004 and 163.9576 assigned to the proton combined similar structure III coordinated with Co^{2+} and Fe^{3+}, respectively. The successfully sulfur coordinated with Co and Fe metal atoms in CoFe LDH, which also confirms the proposed mechanism (**Fig. 2A**). Notably, the *v*-CoFe LDH exhibited a very low overpotential of 330 mV at the current density of 50 mA cm^{-2} compared with CoFe LDH of 360 mV and showed a lower Tafel slope of 44.7 mV dec^{-1}, superior to 52.3 mV dec^{-1} for CoFe LDH (Fig. S29). Hence, this facile organic anchor strategy can be generally used to TM LDHs, and can be extended to other materials besides LDHs used here.

Then, the structural configurations of the stable adsorption of intermediates have been demonstrated (**Fig. 7A**). The metal sites near the defective region not only demonstrates high electroactivity but also play a key role in stabilizing the intermediates for efficient transformation during OER. The energetic trend of the OER pathway is also investigated (**Fig. 7B**). Under the standard potential (U= 0 V) the OER process shows the continuous uphill trend. The reaction of [$3OH^-$ + *OH] to [$2OH^-$ + H_2O + O*] shows an energy barrier of 1.24 eV. The largest barrier of the OER occurs for the transformation of [O*] to [*OOH], which exhibits an

energy barrier of 1.46 eV, indicating the rate-determining step (RDS). With the applied potential of U = 1.23 V, the strong binding of *OH becomes energetically favorable with an energy release of 0.31 eV (**Fig. 7C**). Moreover, the overbinding of *OH leads to the overpotential of 0.23 V, which is close to the experimental results for the overpotential. Furthermore, we have compared the formation of vacancy under different conditions (**Fig. 7D**). The formation of metal vacancies is high energetically preferred under the O-poor condition. In comparison, the OH vacancy formation meets a large energy barrier under the O-rich condition. Among the defects, the combination of metal and O vacancies ($V_{Fe+Ni+OH}$) also demonstrate a relatively preferred formation trend, indicating the potential co-existence of both combined vacancies through the synthesis. Therefore, our work has interpreted the improved OER performances induced by the combination of both metal and O vacancies in the lattice.

Conclusion

In summary, we have firstly developed a novel strategy to precisely modify the particular atomic structure of bulk LDH with a specific electron-withdrawing and atom-nabbing organic molecule CH_3NCS to create metal and oxygen dual vacancies in LDH matrix. The HRTEM, XPS and XAS analysis reveal the existence of the Ni, Fe and O vacancies in the *v*-NiFe LDH catalyst resulting in significant promotion of OER performance. The laminar LDH targeted by CH_3NCS achieved markedly enhanced OER activity, characterized by the much lower OER overpotential and Tafel slope. DFT calculations unraveled the significant contribution of the metal vacancies to the improved OER performance, which substantially enhances the electroactivity for binding with adsorbates with efficient electron transfer. Moreover, the electrocatalytic activity of Ni sites near the vacancies have been promoted and further preserved by the neighboring Fe sites to guarantee the efficient and robust OER for the long-term and stable application. Overall, this work sheds light on the design of catalysts with multivacancies for efficient OER catalysis.

Methods

Material synthesis

Synthesis of starting product. NiFe LDHs nanosheets were synthesized by hydrothermal method. In a typical experiment, 0.145 ml of 1 M ferrous chloride ($FeCl_3$) aqueous solution and 0.725 ml of 1 M nickel chloride ($NiCl_2$) aqueous solution were mixed in the beaker with 70.8 ml DI water. Then 5.6 ml of 0.5 M urea aqueous solution and 2 ml of 0.01 M trisodium citrate (TSC) were added into the beaker under magnetic stirring. The mixed solution was then transferred to a 100 ml Teflon lined stainless steel autoclave and capped tightly for hydrothermal reaction in an oven at 150 °C for 24 h. After reaction, the powder was collected by repetitive centrifugation at 7500 rpm for 10 min and washed several times by de-ionized (DI) water and high purity ethanol, then dried at 60 °C in oven overnight.

Synthesis of LDH with multivacancies (v-NiFe LDH). The obtained NiFe LDH was kept

stirring at 75 degree and reacted with different concentration of CH_3NCS (0.1, 0.5, 1.0, 1.25M). As followed, the powder was collected by repetitive centrifugation at 7500 rpm for 10 min and washed several times by DI water and high purity ethanol alternately, then dried at 60 °C in oven overnight. The slurry solution was selected, and meanwhile the *v*-NiFe LDH was obtained.

Synthesis of ultrafine monolayer (L-LDH). An 20 mL aqueous solution containing $Ni(NO_3)_2 \cdot 6H_2O$ (0.2181 g) and $Fe(NO_3)_3 \cdot 9H_2O$ (0.1010) as added dropwise to an aqueous 23 vol.% formamide solution (20 mL) under magnetic stirring at 80 °C. Simultaneously, 0.25 M NaOH solution was added dropwise to maintain a pH of ~10. The reaction was completed within 10 min. After cooling to room temperature, the product was collected by centrifugation, washed repeatedly with DI, and then kept in a wet state for subsequent use.[48,49]

Synthesis of L-LDH with multivacancies (v-L-LDH). The synthesis of *v*-L-LDH was similar to that presented above for *v*-NiFe LDH, except that the original LDH was L-LDH instead.

Characterizations

The composition of the washed structure and LDHs were analyzed by the inductively coupled plasma (ICP) atomic emission spectroscopy (JarrelASH, ICAP-9000). The samples were dissolved in a dilute acid solution and filtered with semipermeable membrane. The catalyst aqueous suspensions were drop-casted onto silicon wafer and the scanning electron microscopy (SEM) images were collected on a Zeiss Ultra 55 SEM at 5.0 kV. Atomic force microscopy (AFM, Multimode Nanoscope IIIa, Veeco Instruments) was used to determine the size and thickness of the LDH materials. The crystal structure of samples was determined by X-ray diffraction (XRD, D8 Advance X-ray diffractometer) operated at 40 kV and 40 mA with a Cu Kα radiation (λ=1.5405 Å) in the 2θ ranging from 10° to 80° with a step size of 0.02°. NMR ^1H and ^{13}C NMR spectra were recorded on Bruker AC 250 and Bruker AV 360 spectrometers (63 and 90 MHz for ^{13}C, respectively). Chemical shifts δ, are reported in ppm taking residual MeOD as the internal reference. ^1H NMR (300MHz, MeOD): δ 2.9 [$-CH_3$]; 4.5 [$-NHCH_3$]; ^{13}C NMR (300MHz, MeOD): δ 29 [$-CH_3$]; 209 [-NHCO]. Mass spectra (MS) were recorded on a Finningan-MAT-95-S, using MeOH/ H_2O (80/20, v/v) as solvent. *m/z* Anal. Calcd. for $C_2H_5NNiO_2S$, $(M+H)^+$ 165.9394, found: 165.9079; for $C_2H_5NFeO_2S$, $(M+H)^+$ 163.9766, found: 163.9129. X-ray photoelectron spectroscopy (XPS) spectra were collected on Thermo ESCALAB 250XI (ThermoScientific). Spectra were analyzed using XPSPEAK software. The C1s peak for adventitious hydrocarbons at 284.8 eV was used for binding energy calibration. XAS measurements were performed at 8-ID beamline of the National Synchrotron Light Source II (NSLS II) at Brookhaven National Laboratory in the transmission mode. The X-ray absorption near edge structure and Extended X-ray absorption fine structure spectra were processed using the Athena software package. The AUTOBK code was used to normalize the absorption coefficient, and separate the EXAFS signal, χ (k), from the isolate atom-absorption background. The extracted EXAFS signal, χ (k), was weighted by k3 to emphasize the high-energy oscillations and then Fourier-transformed in a k range from

3.0 to 12.5 $Å^{-1}$ to analyze the data in R space. Total scattering pair distribution function experiments were carried out at beamline 28-ID-2 at NSLS-II of BNL using an X-ray energy of 66.7 keV (λ = 0.185794 Å) and an amorphous silicon area detector (Perkin-Elmer) to obtain data to large momentum transfer values. Data were integrated using the program Fit2D. PDFgetX3 was used to correct the data for background contributions, Compton scattering and detector effects, and to Fourier transform (Qmax = 23.5 Å) the data to generate G(r), the PDF.

Preparation of catalyst Ni foam electrodes

1 mg catalyst was dispersed in 0.25 ml ethanol by sonication for 2 hours uniformly, then mixed with 0.25 ml 4% PTFE. The catalyst ink was dropped onto a piece of Ni foam (1 cm × 1 cm) homogeneously after sonication for 30 min, and then dried in oven at 60 ℃ for 15 min to obtain catalyst Ni foam electrode. Before dropped, the Ni foam was immersed in 1 M HCl solution for 10 min to remove the surface oxide, and washed by DI and ethanol for several times and then dried in oven at 60 ℃.

Electrochemical tests

Electrochemical measurements were carried out in a standard three electrode system conducted by a CHI 660D electrochemistry workstation. The as-prepared catalyst Ni foam was used as the working electrode, platinum wire as the counter electrode and Hg/HgO electrode as the reference electrode. The reference was calibrated against and converted to reversible hydrogen electrode (RHE). All measurements were recorded in 1 M KOH. The cyclic voltammetry (CV) measurements were cycled at a scan rate of 10 mV s^{-1} until a stable CV curve was achieved before measuring polarization curves of the catalysts. Linear sweep voltammetry (LSV) was carried out at 5 mV s^{-1} for the polarization curves and 1 mV s^{-1} for Tafel plots. LSV polarization curves were corrected with 95 % iR-compensation.[50] Chrompotentiometry (CP) was carried out under a constant current density of 50 mA cm^{-2}. Electrochemical impedance spectroscopy (EIS) analysis were conducted at 0.25 V vs RHE at DC potential of 10 mV with the frequency ranging from 100 kHz to 0.1 Hz. The electrochemically active surface areas (ECSAs) were evaluated from the electrochemical double-layer capacitance (C_{dl}), which was collected by recording CV values at different scan rates (4, 6, 8, and 10 mV·s^{-1}) in the potential range from 1.02 to 1.12 V versus RHE. The amounts of O_2 evolution (nO_2) experimentally were tested under constant oxidation current of 20 mA for different times by GC2014 (Shimadzu, Japan). And the theoretically generated oxygen contents were determined using Faraday's laws of electrolysis as follows: $nO_2' = Q/4F = I \times t/4F$, where Q is measured charge, I is a constant oxidation current, t is the active time at the constant oxidation current, and F is Faraday constant, 96485 C/mol. The Faradaic efficiency was calculated to be 97.1 %.

Calculation setup

For all the calculations in this work, we have selected the density functional theory (DFT) within the CASTEP package for all the explorations of electronic structures and energetic

reaction pathways.[51] To describe the exchange-correlation energy, the generalized gradient approximation (GGA) with Perdew-Burke-Ernzerhof (PBE) is applied for all the calculations.[52-54] The cutoff energy within the plane-wave set has been set to 380 eV based on the ultrafine quality of the ultrasoft pseudopotential scheme.[55] The coarse k-point has been applied for the energy minimization based on the Broyden-Fletcher-Goldfarb-Shannon (BFGS) algorithm.[56,57] For all the models, we have set the vacuum space of 20 Å along the z-axis to guarantee sufficient space for geometry relaxation and intermediate adsorptions.

For the valence states of Ni, Fe, O and H atoms, we choose the projector-based (*3d, 4s, 4p*), (*3d, 4s, 4p*), (*2s, 2p*) and (*1s*) states, respectively. To reach the ground-state geometry optimization, we have set the convergence test as: the Hellmann-Feynman forces should be converged to less than 0.001 eV/Å; the total energy has been converged to 5×10^{-5} eV per atom; the maximum stress and maximum displacement should not exceed 0.2 GPa and 0.005 Å, respectively.

Conflict of Interest

The authors declare that they have no known competing financial interests or personal relationships that could have appeared to influence the work reported in this paper.

Author contributions

Y.W., J.H. and S.Y. designed the experiment. M.S. and B.H. performed the density functional theory calculations. Y.W. conducted the experiment with the help of S.T. and K.Z. (XANES characterizations and Analysis), K.T. and R.C (AFM tests), H.L. and G.W. (NMR tests). M.S. and B.H. performed the DFT calculations and wrote parts of the manuscript. Y.W., J.H., B.H., C.Z. and S.Y. analyzed the data and wrote the manuscript. All the authors discussed the results and commented on the manuscript.

Acknowledgements

This work was financially supported by China Postdoctoral Fund (2019M660331), the Shenzhen Peacock Plan Program (KQTD2016053015544057), the Nanshan Pilot Plan (LHTD20170001), the NFSC/Hong Kong RGC Research Scheme (N_HKUST610/14), the RGC of Hong Kong (GRF No. 16312216), the HK Innovation and Technology Fund (GHP/079/17SZ), National Nature Science Foundation of China (Nos. 21862011, 51864024) and Yunnan province (2019FI003).

Reference

[1] M.G. Walter, E.L. Warren, J.R. McKone, S.W. Boettcher, Q. Mi, E.A. Santori, N.S. Lewis, Chem. Rev., 110 (2010) 6446-6473.

[2] B.M. Hunter, H.B. Gray, A.M. Müller, Chem. Rev., 116 (2016) 14120-14136.

[3] Y. Zhou, J.L. Silva, J.M. Woods, J.V. Pondick, Q. Feng, Z. Liang, W. Liu, L. Lin, B. Deng, B. Brena, F. Xia, H. Peng, Z. Liu, H. Wang, C.M. Araujo, J.J. Cha, Adv. Mater., 30 (2018) 1706076.

[4] M.T.M. Koper, Chem. Sci., 4 (2013) 2710-2723.

[5] Y. Li, B. Huang, Y. Sun, M. Luo, Y. Yang, Y. Qin, L. Wang, C. Li, F. Lv, W. Zhang, S. Guo, Small, 15 (2019) 1804212.

[6] K. Fan, H. Chen, Y. Ji, H. Huang, P.M. Claesson, Q. Daniel, B. Philippe, H. Rensmo, F. Li, Y. Luo, L. Sun, Nat. Commun., 7 (2016) 11981.

[7] J. Ping, Y. Wang, Q. Lu, B. Chen, J. Chen, Y. Huang, Q. Ma, C. Tan, J. Yang, X. Cao, Z. Wang, J. Wu, Y. Ying, H. Zhang, Adv. Mater., 28 (2016) 7640-7645.

[8] X. Long, Z. Wang, S. Xiao, Y. An, S. Yang, Mater. Today, 19 (2016) 213-226.

[9] J. Yu, Q. Cao, Y. Li, X. Long, S. Yang, J.K. Clark, M. Nakabayashi, N. Shibata, J.-J. Delaunay, ACS Catalysis, 9 (2019) 1605-1611.

[10] Y. Wang, D. Yan, S. El Hankari, Y. Zou, S. Wang, Advanced Science, 5 (2018) 1800064.

[11] L. Trotochaud, J.K. Ranney, K.N. Williams, S.W. Boettcher, J. Am. Chem. Soc., 134 (2012) 17253-17261.

[12] I.J. Godwin, M.E.G. Lyons, Electrochem Commun., 32 (2013) 39-42.

[13] R.L. Doyle, I.J. Godwin, M.P. Brandon, M.E.G. Lyons, Phys. Chem. Chem. Phys., 15 (2013) 13737-13783.

[14] X. Zhang, Z. Lai, Q. Ma, H. Zhang, Chem. Soc. Rev., 47 (2018) 3301-3338.

[15] J. Liu, Y. Zheng, Z. Wang, Z. Lu, A. Vasileff, S.-Z. Qiao, Chem. Commun., 54 (2018) 463-466.

[16] Y. Qu, L. Wang, Z. Li, P. Li, Q. Zhang, Y. Lin, F. Zhou, H. Wang, Z. Yang, Y. Hu, M. Zhu, X. Zhao, X. Han, C. Wang, Q. Xu, L. Gu, J. Luo, L. Zheng, Y. Wu, Adv. Mater., 31 (2019) 1904496.

[17] Y. Sun, S. Gao, F. Lei, Y. Xie, Chem. Soc. Rev., 44 (2015) 623-636.

[18] T. Ling, D.-Y. Yan, Y. Jiao, H. Wang, Y. Zheng, X. Zheng, J. Mao, X.-W. Du, Z. Hu, M. Jaroniec, S.-Z. Qiao, Nat. Commun., 7 (2016) 12876.

[19] Q. He, H. Xie, Z.u. Rehman, C. Wang, P. Wan, H. Jiang, W. Chu, L. Song, ACS Energy Lett., 3 (2018) 861-868.

[20] S. Choi, Y. Park, H. Yang, H. Jin, G.M. Tomboc, K. Lee, CrystEngComm, 22 (2020) 1500-1513.

[21] R. Zhang, Y.-C. Zhang, L. Pan, G.-Q. Shen, N. Mahmood, Y.-H. Ma, Y. Shi, W. Jia, L. Wang, X. Zhang, W. Xu, J.-J. Zou, ACS Catal., 8 (2018) 3803-3811.

[22] D. Zhou, X. Xiong, Z. Cai, N. Han, Y. Jia, Q. Xie, X. Duan, T. Xie, X. Zheng, X. Sun, X.

Duan, Small Methods, 2 (2018) 1800083.

[23] M. Asnavandi, Y. Yin, Y. Li, C. Sun, C. Zhao, ACS Energy Lett., 3 (2018) 1515-1520.

[24] J. Suntivich, K.J. May, H.A. Gasteiger, J.B. Goodenough, Y. Shao-Horn, Science, 334 (2011) 1383.

[25] Y. Wang, Y. Zhang, Z. Liu, C. Xie, S. Feng, D. Liu, M. Shao, S. Wang, Angew. Chem. Int. Edi., 56 (2017) 5867-5871.

[26] C. Meng, M. Lin, X. Sun, X. Chen, X. Chen, X. Du, Y. Zhou, Chem. Commun., 55 (2019) 2904-2907.

[27] I.S. Cho, M. Logar, C.H. Lee, L. Cai, F.B. Prinz, X. Zheng, Nano Lett., 14 (2014) 24-31.

[28] P. Zhou, Y. Wang, C. Xie, C. Chen, H. Liu, R. Chen, J. Huo, S. Wang, Chem. Commun., 53 (2017) 11778-11781.

[29] B.M. Hunter, W. Hieringer, J.R. Winkler, H.B. Gray, A.M. Müller, Energy Environ. Sci., 9 (2016) 1734-1743.

[30] M. Rajakumar, M. Manickam, N.N. Gandhi, K. Muthukumar, Int. J. Hydrogen Energy, 45 (2020) 3905-3915.

[31] D. Nikolova, R. Edreva-Kardjieva, G. Gouliev, T. Grozeva, P. Tzvetkov, Appl. Catal. A., 297 (2006) 135-144.

[32] J. Grimblot, P. Dufresne, L.G. And, J.-P. Bonnelle, B. Soc. Chem. Belges, 90 (1981) 1261-1269.

[33] T.-C. Lin, G. Seshadri, J.A. Kelber, Appl. Surf. Sci., 119 (1997) 83-92.

[34] R.V. Siriwardane, J.M. Cook, J. Colloid Interf. Sci., 108 (1985) 414-422.

[35] P. Xu, W. Zeng, S. Luo, C. Ling, J. Xiao, A. Zhou, Y. Sun, K. Liao, Electrochim. Acta, 241 (2017) 41-49.

[36] K. Uvdal, P. Bodö, B. Liedberg, J. Colloid Interf. Sci., 149 (1992) 162-173.

[37] H.E. Gottlieb, V. Kotlyar, A. Nudelman, J. Syn. Organ. Chem., 62 (1997) 7512-7515.

[38] L.I. Kasyan, A.O. Kasyan, I.N. Tarabara, S.I. Okovytyy, E.A. Golodayeva, A.V. Tokar, Y. Podolyan, Cent. Eur. J. Chem., 6 (2008) 161-174.

[39] I. Jarraya, I. Abdelhedi, M. Abid, S. Abid, R.E. Gharbi, Mediterranean J. Chem., 2 (2014) 708-719.

[40] C. Fringant, M. Rinaudo, M.F. Foray, M. Bardet, Carbohyd. Polym., 35 (1998) 97-106.

[41] T. Nishiwaki, E. Kawamura, N. Abe, M. Iori, J. Chem. Soc. Pakistan, (1980) 2693-2699.

[42] Y. Wang, M. Qiao, Y. Li, S. Wang, Small, 14 (2018) 1800136.

[43] S. Nayak, K.M. Parida, ACS Omega, 3 (2018) 7324-7343.

[44] S. Dutta, A. Indra, Y. Feng, T. Song, U. Paik, ACS Appl. Mater. Inter., 9 (2017).

[45] Y. Zhao, X. Zhang, X. Jia, G.I.N. Waterhouse, R. Shi, X. Zhang, F. Zhan, Y. Tao, L.-Z. Wu, C.-H. Tung, D. O'Hare, T. Zhang, Adv. Energy Mater., 8 (2018) 1703585.

[46] L. Tian, K. Wang, H. Wo, Z. Li, M. Song, J. Li, T. Li, X. Du, Journal of the Taiwan Institute of Chemical Engineers, 96 (2019) 273-280.

[47] D. Ji, S. Peng, L. Fan, L. Li, X. Qin, S. Ramakrishna, Journal of Materials Chemistry A, 5 (2017) 23898-23908.

[48] J. Yu, B.R. Martin, A. Clearfield, Z. Luo, L. Sun, Nanoscale, 7 (2015) 9448-9451.

[49] X. Zhang, Y. Zhao, Y. Zhao, R. Shi, G.I.N. Waterhouse, T. Zhang, Adv. Energy Mater., 9 (2019) 1900881.

[50] M. Gong, Y. Li, H. Wang, Y. Liang, J.Z. Wu, J. Zhou, J. Wang, T. Regier, F. Wei, H. Dai, J. Am. Chem. Soc., 135 (2013) 8452-8455.

[51] J.C. Stewart, D.S. Matthew, J.P. Chris, J.H. Phil, I.J.P. Matt, R. Keith, C.P. Mike, Zeitschrift für Kristallographie - Crystalline Materials, 220 (2005) 567-570.

[52] J.P. Perdew, K. Burke, M. Ernzerhof, Phys. Rev. Lett., 77 (1996) 3865-3868.

[53] P.J. Hasnip, C.J. Pickard, Comput. Phys. Commun., 174 (2006) 24-29.

[54] J.P. Perdew, J.A. Chevary, S.H. Vosko, K.A. Jackson, M.R. Pederson, D.J. Singh, C. Fiolhais, Physical Review B, 46 (1992) 6671-6687.

[55] D. Vanderbilt, Physical Review B, 41 (1990) 7892-7895.

[56] J.D. Head, M.C. Zerner, Chem. Phys. Lett., 122 (1985) 264-270.

[57] M.I.J. Probert, M.C. Payne, Physical Review B, 67 (2003) 075204.

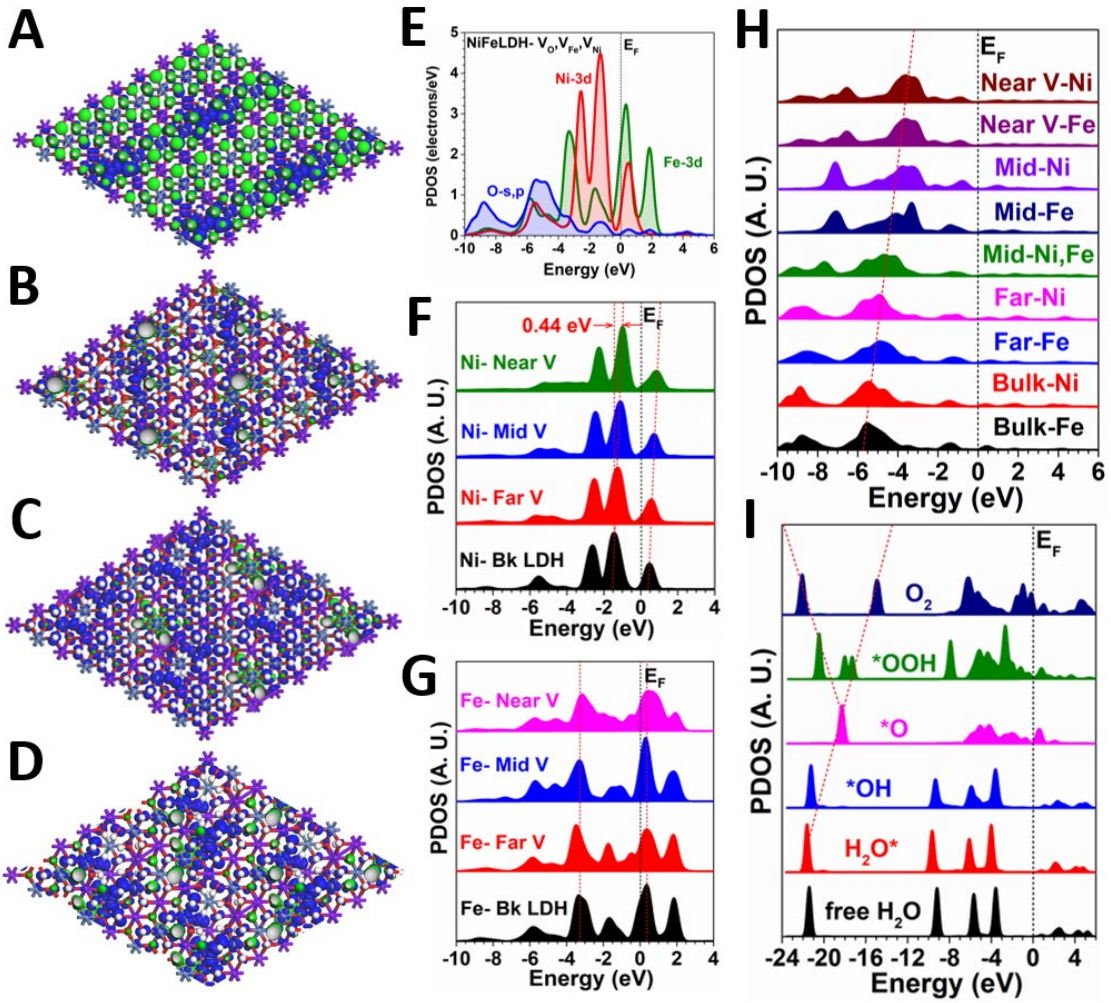

Fig. 1. The electronic structure of the defective NiFe LDH. The 3D contour plot of bonding and anti-bonding near Fermi level for **(A)** NiFe LDH with OH vacancy. **(B)** NiFe LDH with Fe vacancy. **(C)** NiFe LDH with Ni vacancy. **(D)** NiFe LDH with Ni, Fe, and O vacancies. **(E)** The PDOSs of NiFe LDH with Ni, Fe, and O vacancies. **(F)** The site-dependent PDOSs of Ni-3d orbitals. **(G)** The site-dependent PDOSs of Fe-3d orbitals. **(H)** The site-dependent PDOSs of O-2p orbitals. **(I)** The PDOSs of intermediates of the OER.

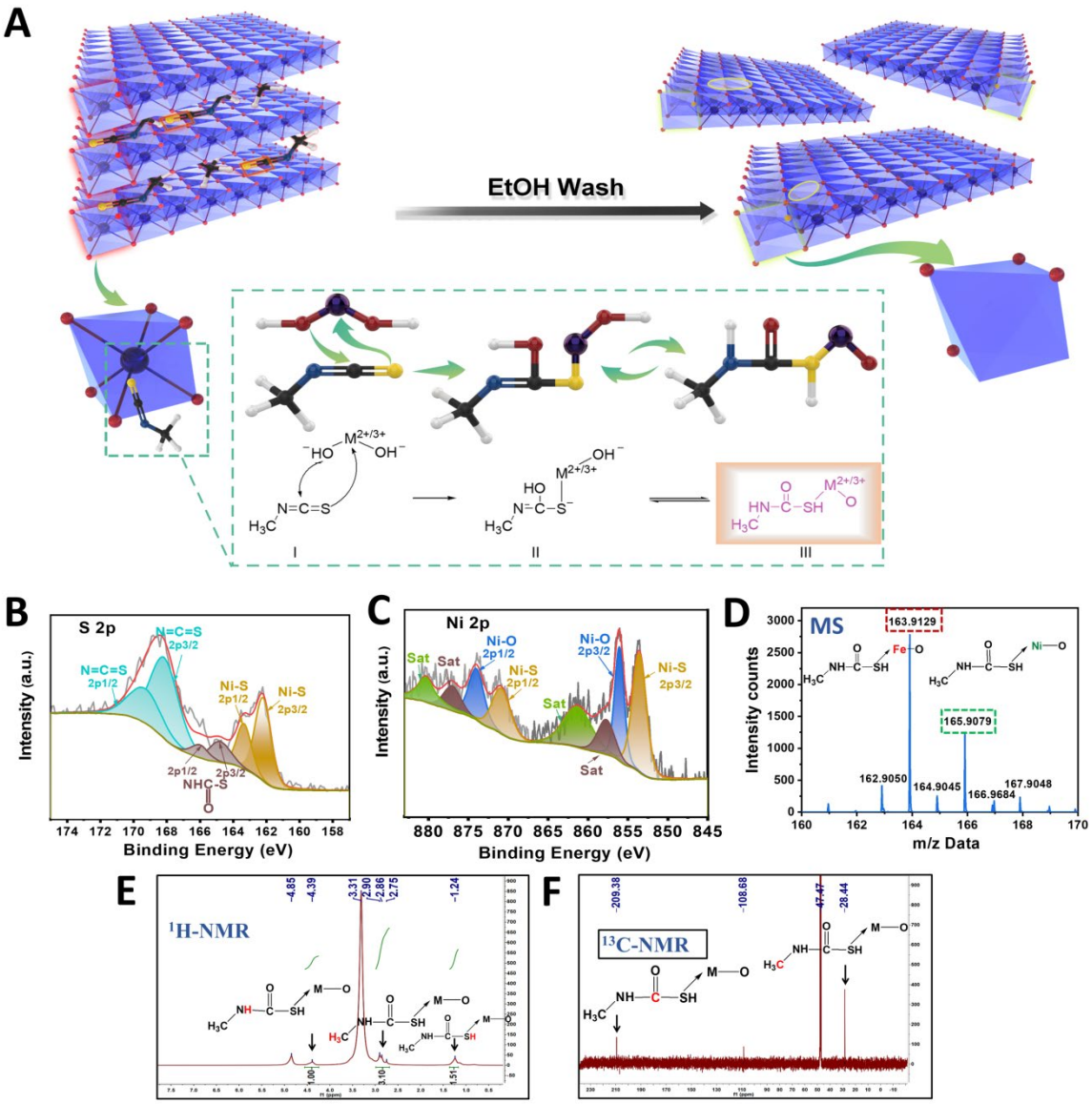

Fig. 2. Design of the NiFe LDH with Metal and Oxygen Multivacancies. (A) The mechanism of targeting specific atoms to create multivacancies. Structure characterizations: high resolution XPS spectra of (**B**) S 2p and (**C**) Ni 2p regions. **(D)** Mass spectra (MS) of the slurry washed by ethanol after NiFe LDH targeted by CH_3NCS. (**E**) ^{1}H-NMR and (**F**) ^{13}C-NMR spectra.

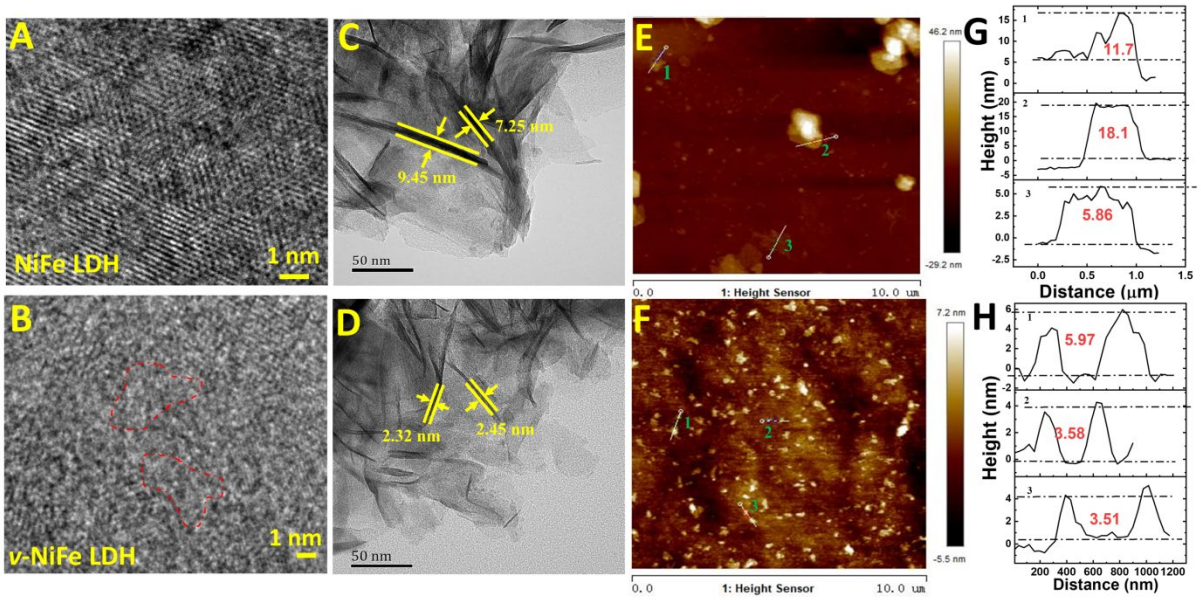

Fig. 3. Microstructure of the NiFe LDH and *v*-NiFe LDH catalysts. High resolution SEM (HRSEM) and TEM images of (**A**&**C**) NiFe LDH and (**B**&**D**) *v*-NiFe LDH. The red circles in B indicate lattice distortions; AFM height profiles of (**E**) NiFe LDH and (**F**) *v*-NiFe LDH; the numbers 1–3 in (**G**&**H**) correspond to the profiles 1–3 in (**E**&**F**).

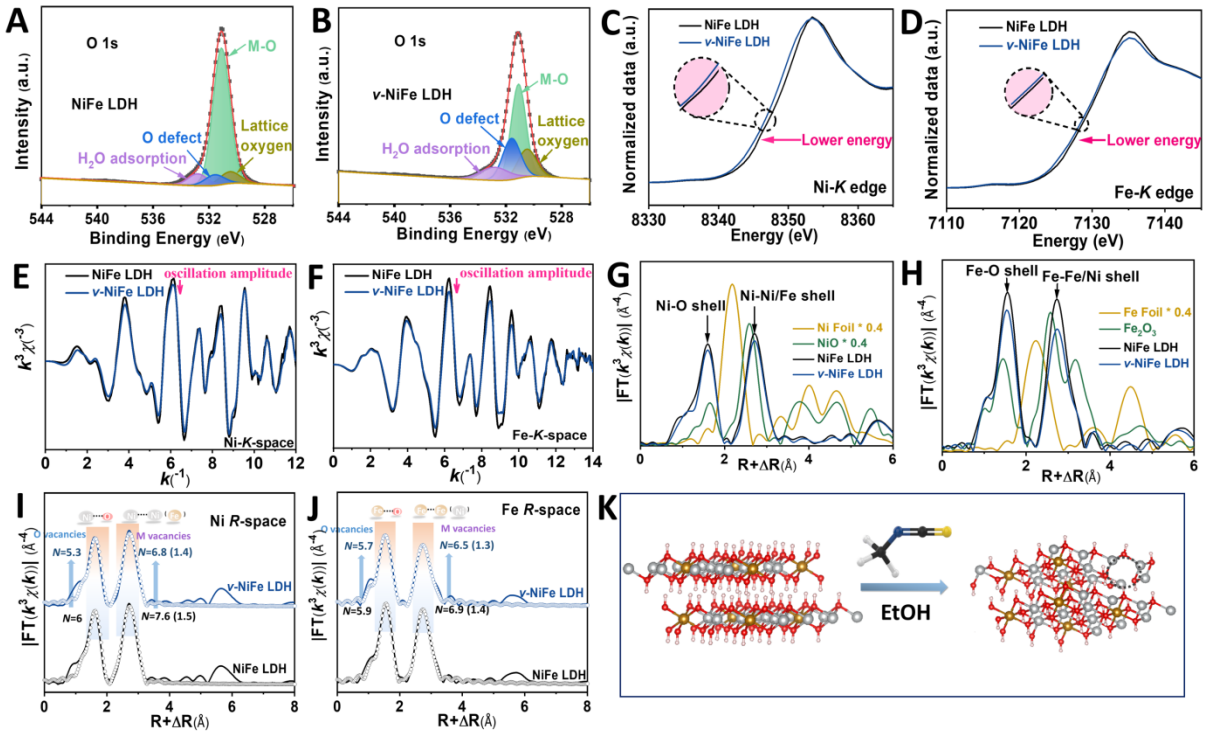

Fig. 4. Analysis of oxygen and metal vacancies of *v*-NiFe LDH. High resolution XPS spectra of (**A**) NiFe LDH and (**B**) *v*-NiFe LDH in O 1s regions. (**C**) Ni K-edge XANES spectra, (**D**) Fe K-edge XANES data, the insets in **C** and **D** show magnified view of the rectangles. (**E**) Ni K-edge EXAFS oscillation functions $k^3\chi(k)$, **(F)** Fe K-edge EXAFS oscillation functions $k^3\chi(k)$, (**G**) detailed structural information shown in the k^3-weighted FT spectra in R-space at the Ni K edge and **(H)** the Fe K edge, and **(I)** the fitted R-space plots at Ni K edge and **(J)** at Fe K edge for pristine NiFe LDH and *v*-NiFe LDH nanosheets. **(K)** Local structual models of NiFe LDH (left), and *v*-NiFe LDH (right); Fe, Ni, O, H, C, N and S atoms are shown in orange, grey, red, white, black, blue, and yellow, respectively.

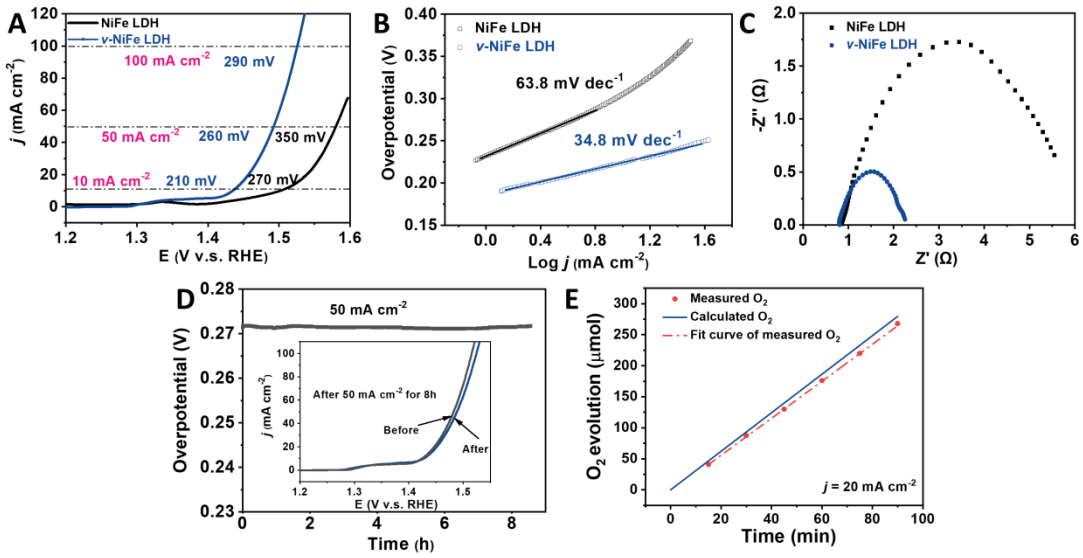

Fig. 5. Electrocatalytic performance characterizations of the catalysts. (A) Linear sweep voltammograms (LSV) curves, **(B)** Tafel plots, and **(C)** Electrochemical impedance spectra (EIS) at the overpotential of 250 mV of NiFe LDH and *v*-NiFe LDH, **(D)** Chronopotentiometry (CP) curves of *v*-NiFe LDH at 50 mA cm^{-2}; inset: the LSV curves before (black) and after (blue) that the CVs were circulated for about 2000 cycles, **(E)** theoretical and experimental tested O_2 evolution on *v*-NiFe LDH.

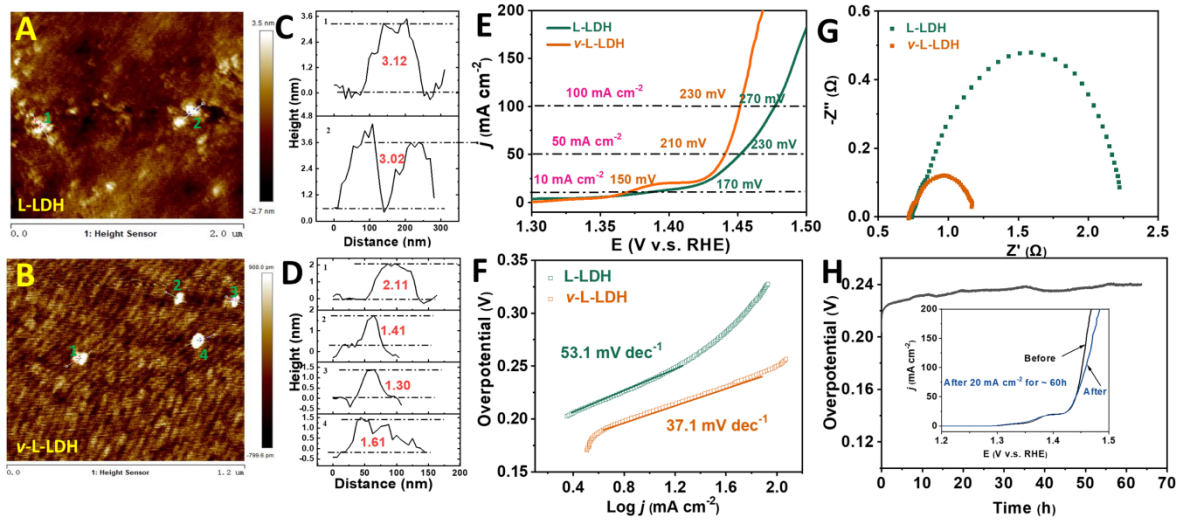

Fig. 6. Characterizations of the laminar NiFe LDH catalyst. AFM height profiles of (**A**) laminar NiFe LDH (L-LDH) and (**B**) L-LDH with multivancancies (*v*-L-LDH) targeted by CH_3NCS treatment; Height protocols in (**C** and **D**) correspond to the profiles 1–2 in **A** and 1–4 in **B**; (**E**) linear sweep voltammograms (LSV) curves of L-LDH and *v*-L-LDH; **(F)** Tafel plots of L-LDH and *v*-L-LDH; (**G**) Electrochemical impedance spectra (EIS) at the overpotential of 250 mV of L-LDH, *v*-L-LDH; **(H)** Chronopotentiometry (CP) curves of *v*-L-LDH at 20 mA cm^{-2}; inset: the LSV curves before (black) and after (blue) the CP test.

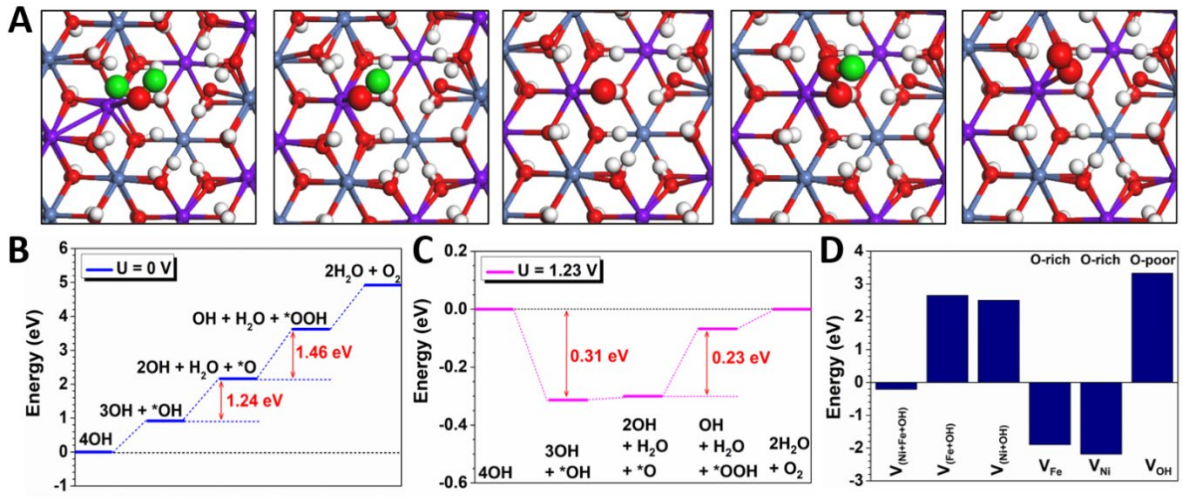

Fig. 7. The energetic reaction trend of the defective NiFe LDH. (**A**) The structural configuration of stable adsorptions for intermediates. Purple balls = Ni atoms, blue balls = Fe atoms, red balls = O atoms, white balls = H atoms in the NiFe LDH, and green balls = H atoms of adsorbates. (**B**) The energetic trend of OER under the standard potential. (**C**) The energetic trend of OER under U = 1.23 V. (**D**) The formation energy comparison of different vacancies.